Photoionization of rare-gas-dimer excited states: Experimental measurements of absolute cross sections for $Xe_2^*(0_u^+, 1_g, 2_g)$ in the ultraviolet ($248 \leq \lambda \leq 351$ nm)

A. W. McCown, M. N. Ediger, and J. G. Eden
University of Illinois, Urbana, Illinois 61801
(Received 18 October 1983)

Photoionization of excited states of the xenon dimer (Xe_2) has been observed and absolute ionization cross sections have been measured for several laser wavelengths between 248 and 351 nm. Production of the excimers is accomplished by two-photon ionization of ground-state Xe atoms at 193 nm, followed by formation and the subsequent dissociative recombination of Xe_2^+ $1(\frac{1}{2})_u$ ions, collisional and radiative relaxation of the Xe $6p$ and $6s'$ manifolds, and formation of low-lying excimer states by three-body collisions. Absolute photoionization cross sections are subsequently determined at 351.1, 337.1, 307.9, 277.0, and 248.4 nm by combining a second rare-gas—halide excimer (or N_2) laser pulse with a microwave-absorption technique to monitor the absolute photoelectron density (in real time) as a function of the intensity of the second laser pulse. The use of microwave absorption allows for the detection of photoelectrons in the presence of a high-pressure background gas. Laser-induced fluorescence and spontaneous emission studies of the temporal behavior of the populations of all of the Xe $6p$ states as well as the $6s'(\frac{1}{2})_0$ and $6s(\frac{3}{2})_1$ levels confirm that a molecule is being photoionized. The molecular states involved are 0_u^+, 1_g, and 2_g which correlate with the $6s(\frac{3}{2})_1$ excited level and a $^1S_0$ (ground-state) atom. The optical transitions associated with each laser wavelength λ studied appear to be Xe_2^* $0_u^+ \rightarrow Xe_2^+$ $1(\frac{3}{2})_g$ ($\lambda = 248.4$ nm); 1_g (or 2_g)$\rightarrow 1(\frac{3}{2})_u$ ($\lambda = 277.0$ nm); and 1_g (or 2_g)$\rightarrow 1(\frac{1}{2})_u$ for $\lambda = 307.9$, 337.1, and 351.1 nm. The discrepancy between the measured cross sections and the values calculated previously (Lorents, Eckstrom, and Huestis, 1973) from a quantum-defect approach is roughly a factor of 2 at 308 nm but increases rapidly at shorter wavelengths. Also, in contrast to theoretical predictions for the $6s$ *atomic* Xe excited states in which the photoionization cross section σ falls monotonically with photon energy, the measured σ peaks at 7×10^{-18} cm^2 for $\lambda = 308$ nm ($\hbar\omega = 4$ eV). The profile of the photoionization cross-section spectrum that is reported here for Xe_2^* is, however, remarkably similar to that calculated by Rescigno *et al.* [J. Chem. Phys. 68, 5283 (1978)] for the $^1\Sigma$ excited state of the Ar_2 excimer (Ar_2^*).

I. INTRODUCTION

One major inducement for studying the photoionization of atomic and molecular rare-gas excited states is its pivotal role in determining electron production and transient self-absorption[1] in rare-gas—buffered lasers. However, despite its importance to an understanding of energy transfer in laboratory plasmas, few experimental measurements of *absolute* photoionization cross sections for the excited states of the rare gases have been made.

A. Photoionization cross sections for atomic rare-gas excited states

By collecting the ions produced at the intersection of a laser and a beam of rare-gas atoms, Stebbings *et al.*[2] and Dunning and Stebbings[3] were able to make the first measurements of the absolute photoionization cross sections for the $2\,^{1,3}S$ and $n\,^{1,3}P$ excited states, respectively, of helium. This work was later extended to the lowest metastable states of Ar, Kr, and Xe but only an upper bound or estimate of the cross section was obtained due to uncertainties in the population of the rare-gas excited state.[4–7] More recently, Bokor *et al.*[8] deduced the photoionization cross section for the $6p[\frac{3}{2}]_2$ state of Kr at 193.3 nm from fluorescence measurements when the state was excited by two ArF excimer-laser photons.

From a theoretical standpoint, early efforts also focused on the $2\,^1S$ and $2\,^3S$ states of helium.[9–12] In 1977, Hyman,[13] McCann and Flannery,[14] and Hazi and Rescigno[15] calculated the spectral dependence of the photoionization cross sections for the low-lying s and p states of the heavier rare gases (Ne—Xe). Since then, studies of the rare-gas s' and d levels[16,17] and reexaminations of the p-state cross sections[18,19] have been carried out as well.

Summarizing the situation in 1979, McDaniel *et al.*[20] stated that "[Absolute] experimental data exist only for the He $2\,^1S$ and $2\,^3S$ metastable states. Reasonably reliable theoretical data exist for the lowest metastable $np^5(n+1)s$ states of Ne, Ar, Kr, and Xe. Experimental data are needed for these cases as well as for other excited states which are metastable or just reasonably long-lived." Even considering Ref. 8 and the more recent theoretical papers, this statement continues to be true.

B. Molecular (dimer) excited states

Even less is known of the photoionization cross sections for the rare-gas-dimer excited states (R_2^*). As noted by McCusker,[21] "The photoionization cross sections for the

excimers have not been directly measured" and the only available theoretical values appear to be those determined for the lowest-lying 0_u and 1_u states by Lorents *et al.*[22] with a quantum-defect approach and *ab initio* calculations for photoionization of $Ar_2^*(^1\Sigma_1)$ reported by Rescigno *et al.*[23] The major obstacle for experimentalists in this area is isolating the particular excited species to be photoionized and to determine the absolute number density in that state. Also, a related and useful diagnostic would be the ability to monitor in real time the number densities of the ions or electrons produced in the photoionization process.

C. Background for present work

In this paper, the development of a novel approach to measuring absolute excited-state photoionization cross sections and its application to xenon are described. Specifically, absolute cross sections for the photoionization of excited states of the xenon dimer (Xe_2) have been determined at several wavelengths in the ultraviolet.

In recent work on photodissociation of the Xe_2^+ $1(\frac{1}{2})_u$ ion,[24] an increase in the electron density was unexpectedly observed when the arrival of an ultraviolet laser pulse at a laser-produced Xe plasma was delayed more than ~ 100—150 ns with respect to the initiation of the plasma. The additional electron production appeared from preliminary measurements to be due to photoionization of an unidentified Xe excited state. For a laser wavelength of 351 nm, the photoionization cross section for this state was determined to be 2.3×10^{-18} cm^2.

Detailed studies of this phenomenon at several points in the ultraviolet are described here. From spontaneous emission and laser-induced fluorescence (LIF) experiments on various low-lying s, s', and p states of Xe, it is concluded that the atomic Xe levels are *not* responsible for the observed photoionization but that, for wavelengths between 277 and 351 nm, it is the 1_u and 2_u molecular states ($T_e \approx 65\,000$ cm^{-1}) that are being photoionized. At 248 nm, photoionization of the Xe_2 0_u^+ (and possibly 0_u^- or 1_u) state (associated with the $Xe\{6s[\frac{3}{2}]_1\}+Xe\{^1S_0\}$ limit) predominates. Consequently, this work constitutes the first measurement of the spectral variation of the absolute photoionization cross section for any rare-gas-excimer state.

D. Experimental approach

Utilizing a microwave-absorption scheme in conjunction with two ultraviolet (uv) excimer lasers, it is possible to monitor in real time the instantaneous increase in electron density, Δn_e, that results from the photoionization of an excited atom or molecule. As mentioned earlier, the application of two excimer lasers to the measurement of the photoabsorption spectrum of the Xe_2^+ $1(\frac{1}{2})_u$ ion has already been demonstrated.[24]

This approach depends on first photoionizing ground-state Xe atoms and allowing the ensuing Xe* $6p$ states to collisionally relax. Excited molecules are subsequently formed by three-body collisions with background gas atoms. A second uv laser pulse then photoionizes the Xe_2^* molecules with the resulting photoelectrons detected by microwave absorption. In order to ensure that only molecular xenon states are being studied, the "ionizing" laser pulse is withheld until the Xe $6p$, $6s'$, and $6s$ populations have fallen below their peak values. Actually, selectivity regarding the excited state to be ionized is available in two ways: (1) relying on collisions to preferentially populate a certain level (i.e., the measurements are taken within a particular time "window") and (2) design of the parameters of the microwave system such that it is especially sensitive to electrons having a particular energy—that is, photoelectrons produced by ionization of a specific excited state. This is a powerful and versatile technique, and is readily adaptable to other systems, such as the atomic (^3P metastables) and molecular levels of mercury and cadmium.

The photoionization cross section and population of the photoionized molecular state are determined at a given wavelength and time delay between the two lasers from measurements of the variation of Δn_e with the intensity I of the second (ionizing) laser pulse. As I is increased, Δn_e rises exponentially and asymptotically approaches a limit or saturated value of Δn_e which is identically equal to the number density of the state being photoionized. The photoionization cross section is then determined from a computer least-squares fit of an exponential to the data. It should be emphasized, however, that the cross section is independent of the *absolute value* of the electron density *but, for increasing laser intensity, only depends on the rate at which* Δn_e approaches the saturated limit ($I\rightarrow\infty$). By taking advantage of the variety of discrete wavelengths that are available throughout the uv from a commercial rare-gas—halide excimer laser, one can in this way examine a large portion of the uv.

One significant aspect of this technique is that, unlike the biased electrode collection method, electrons are viewed immediately upon being freed from the atom or molecule. This has several important consequences. First, we are able to measure an absolute *increase* in the electron density: i.e., background electrons can be present. Second, since the electron-density increase can be measured at any point in time, it is straightforward to examine the time evolution of Δn_e in order to facilitate identification of the excited state being ionized. *Finally, it is essential that the photoelectron detection method be capable of monitoring the electron density in a high-pressure ambient since dimers only exist in significant concentrations in this environment. This advantage is inherent to microwave absorption.* Consequently, qualitative fluorescence techniques can be avoided.

This paper is organized in the following manner. Section II describes the experimental apparatus and data acquisition techniques that underlie these studies. Section III presents the theoretical considerations relevant to the interpretation of the microwave-absorption (electron density) waveforms and determination of the photoionization cross section. The experimental results are presented in Sec. IV. Specifically, representative microwave-absorption oscillograms are shown. From such electron-density waveforms, the temporal history of the number density of the species being ionized is determined. Comparing this with the results of laser-induced fluorescence and spontaneous emission measurements of the popula-

tions of a large number of Xe $6s$, $6s'$, and $6p$ atomic states leads to the conclusion that the species in question is molecular, not atomic. The section concludes with cross-sectional data taken at several wavelengths in the uv. A detailed discussion of the kinetics involved and a comparison of the experimentally-determined Xe_2^* cross sections with existing theoretical predictions are the subjects of Sec. V, while Sec. VI concludes with a discussion of the photoionization cross sections, possible extension of the experimental technique to the study of other rare-gas-excimer states, and the impact of the data on existing ultraviolet lasers.

II. APPARATUS AND DATA ACQUISITION

A. Experimental setup

A partial schematic diagram of the experimental apparatus for measuring the photoionization cross sections is given in Fig. 1. The setup consists of two excimer lasers (Lambda Physik—EMG 101 and 102) and a microwave-absorption system. One laser operates on the ArF band at 193 nm and the other is equipped with an unstable resonator suitable for operation at any one of several rare-gas—halide excimer wavelengths (XeF, XeCl, or KrF). In addition, the use of a stable optical cavity on the latter laser allowed for experiments to be conducted at 337.1 nm (N_2).

As illustrated in Fig. 1, stimulated Raman scattering (SRS) of KrF in H_2 ($\Delta\tilde{\nu}=4155$ cm^{-1}) provided a fifth wavelength for study. Only the first Stokes line (S_1) at 277.0 nm, however, contained enough energy (>10 mJ) to produce photoelectron densities sufficiently large for accurate and reproducible measurements to be made. Therefore, S_1 was spatially separated from the pump (and five other Stokes and two anti-Stokes wavelengths) by dispersing the beam with a quartz Brewster's angle prism. The 277-nm radiation was then aligned so as to counterpropagate with the ArF laser beam. Cylindrical lenses focused the two rectangular ($\sim 0.2\times 2.9$ cm^2) laser beams to a single line along the axis of a suprasil quartz tube containing 300 Torr of research grade xenon.

The relative times at which the two uv laser pulses arrived at the Xe cell (ArF laser fired first-second laser typically delayed by 300 ns) were controlled by a digital delay generator and a triggering network. Also, the shot-to-shot variations ($<10\%$) in the pulse energy of each laser were monitored by reflecting a known fraction of each beam onto a calibrated photodiode or a Gen-Tec ED500 energy detector. Approximately 40% of the excimer laser pulse

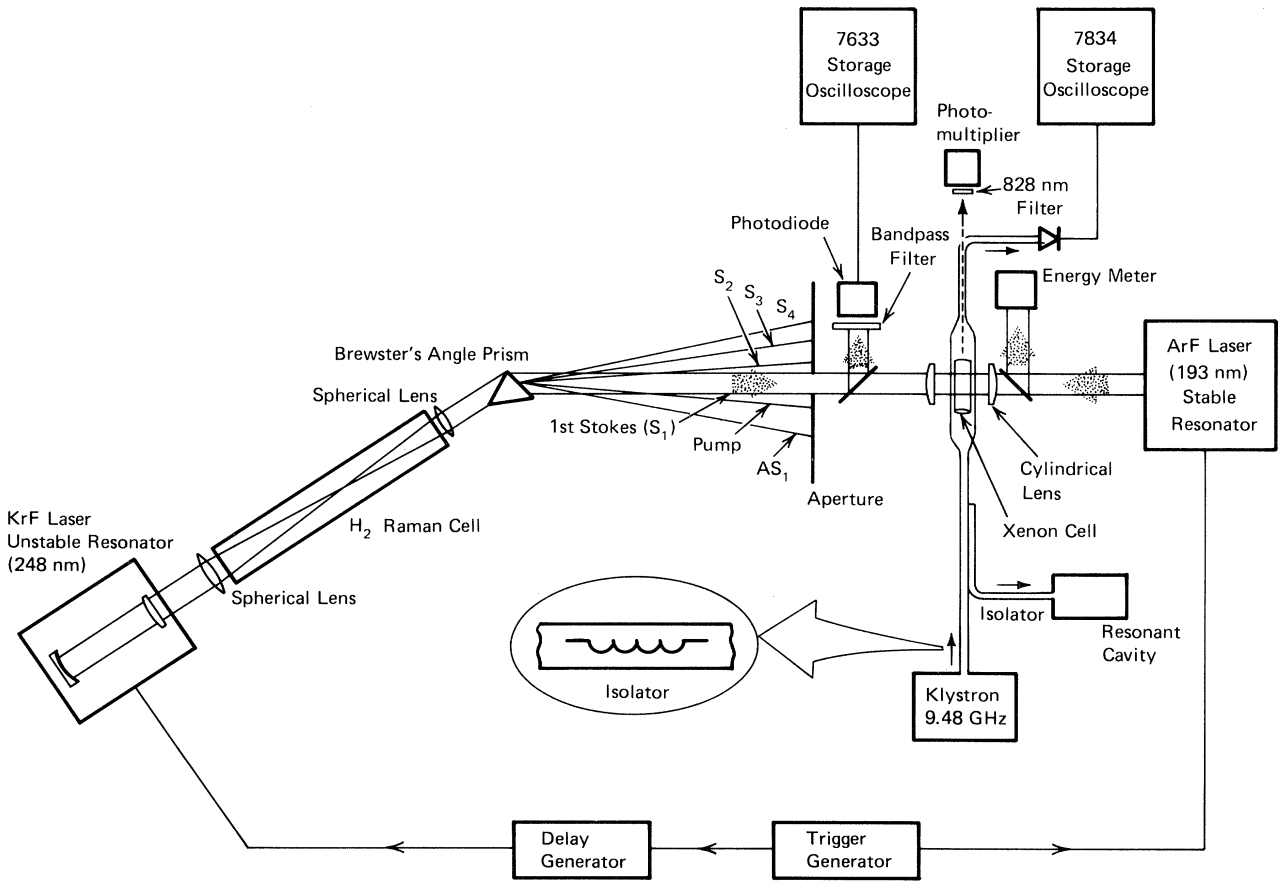

FIG. 1. Experimental apparatus used to measure the absolute photoionization cross section for the lowest $1g,2g$, states of Xe_2 at 277 nm (wavelength of the first Stokes line of the KrF laser in H_2). The microwave bridge, with which the collision frequency for momentum transfer ν_m was measured, is not shown here. Also, for spectral survey measurements, the 828-nm interference filter and photomultiplier were replaced by a 0.6-m Hilger-Engis spectrograph and an optical multichannel analyzer (OMA).

energy was lost at the prism, 7% at the beamsplitter, and 15% at the lens and wall of the Xe cell. The measured laser intensities were, of course, corrected to account for these losses. For each wavelength studied, the excimer oscillators were untuned—thus the laser linewidth was $\sim 100\ \mathrm{cm}^{-1}$ for all experiments and the temporal width of individual pulses was typically 12-ns full width at half maximum (FWHM).

The photodiode monitoring the laser energy was calibrated by recording the photodiode signal versus the actual energy measured by a pyroelectric energy meter directly in the beam. Apertures and/or neutral density filters were placed in front of the photodiode to maintain operation of the detector in the nonsaturated regime.

The Xe cell was placed inside a section of cylindrical waveguide that was slotted on both sides to permit the entry of the laser beams as well as to spatially define the irradiated region. Tapered guide sections interfaced the cylindrical section to WR90 rectangular waveguide. A low-power cw microwave signal at 9.477 GHz was produced by a klystron, and propagated through the laser-produced Xe plasma. The attenuated signal was then detected by a silicon diode and displayed on a Tektronix 7834 storage oscilloscope. A 6-mm-diam hole drilled in an E bend of the waveguide allowed for the Xe excited-state fluorescence to be monitored by an RCA C31034A (GaAs photocathode) photomultiplier and a second storage oscilloscope.

Further details concerning the degassing and filling of the Xe cell and calibration and operation of the optical system can be found in earlier publications.[24–26] Careful superposition and spatial filtering of the two rectangular excimer laser beams at the optical cell, thorough bakeout of the cell and impurity gettering of the xenon were necessary to ensure reproducible results from the experiments.

B. Data acquisition technique

As will be discussed in the next section, once the collision frequency for electron-neutral momentum transfer ν_m in a particular gas is known for a specific electron energy, then the electron number density can be calculated from the experimentally measured attenuation of a microwave signal by the free electrons. Therefore, with the wavelength of the second laser at 277 nm, for example, and the ArF laser (focal) intensity fixed at $\sim 100\ \mathrm{MW\,cm}^{-2}$, microwave attenuation waveforms were recorded for various values of 277-nm laser intensity. Armed with the equations presented in the next section, the electron density at any point in time could then be calculated. Of particular interest is the instantaneous jump in the electron density, denoted as Δn_e, that occurs upon the arrival of the second laser pulse at the optical cell when the time delay between the two pulses was greater than 120–150 ns.[24] As mentioned earlier, by measuring Δn_e as a function of the intensity of the 277-nm laser, the absolute photoionization cross section can be determined. Furthermore, for large laser intensities, Δn_e saturates which allows for the number density of the state(s) being ionized to be determined. Similar experiments were conducted at the other wavelengths studied (248, 308, 337, and 351 nm) except that Raman conversion of the excimer laser output was no longer necessary. In order to maintain a constant beam cross section at the Xe cell, data at 248 and 308 nm were taken with the laser in the same position but with the Raman converter removed. For $\lambda = 351$ nm (XeF), the laser on the left-hand side of Fig. 1 was oriented in such a way that its output was again colinear with the ArF 193-nm beam.

III. THEORETICAL ANALYSIS

A. Review of microwave relations: Photoionization of ground-state Xe atoms

A thorough analysis of the microwave-absorption method for determining peak photoelectron densities has been given elsewhere[25] and will only be briefly reviewed here. The attenuation α and phase shift $\Delta\phi$ suffered by a microwave field traversing a plasma are dependent upon the plasma frequency ω_p (electron density) and the electron-neutral collision frequency ν_m (electron temperature and gas concentration). Consequently, once ν_m is known, the temporally-resolved microwave attenuation waveform can be calibrated to give the absolute electron density at any point in time.

With a microwave bridge (not shown in Fig. 1) incorporated into the apparatus shown earlier and only the ArF laser irradiating the Xe cell, ordered pairs of $\Delta\phi$ and α were determined for the microwave field impinging on the laser plasma produced by two-photon ionization of Xe. In the presence of large background gas densities, the electron-neutral collision frequency is then expressed as

$$\nu_m = \frac{2\alpha\beta\omega}{\alpha^2+(\beta_g^2-\beta^2)}\ , \tag{1}$$

where ω is the radian frequency of the microwave field ($5.95\times10^{10}\ \mathrm{s}^{-1}$), and β_g is the propagation constant in the absence of electrons. The plasma propagation constant β is related to β_g and $\Delta\phi$ by

$$\beta_g-\beta=\frac{\Delta\phi}{L}\ , \tag{2}$$

where L is the plasma length (2.9 cm). Using an adjustable transmission line short, β_g was found to be $1.532\ \mathrm{cm}^{-1}$. Inserting these measured parameters and the ordered pairs of α and $\Delta\phi$ into Eqs. (1) and (2), the average ν_m was determined to be $3.3\times10^{10}\ \mathrm{s}^{-1}$ for 0.7-eV electrons in 300 Torr of Xe.

The expression for the collision frequency was derived from a solution of Maxwell's equations for an ionized gas in a waveguide. The plasma frequency was solved for in a similar manner. The result is

$$F\omega_p^2=2\alpha^2c^2\frac{\nu_m^2+\omega^2}{\nu_m^2}\left[-1+\left[1+\frac{\nu_m^2}{\alpha^2\omega^2}(\alpha^2+\beta_g^2)\right]^{1/2}\right]. \tag{3}$$

The factor F is expressed as

$$F=\frac{\int_s f(\rho,\phi)E_0^2\,dS}{\int_s E_0^2\,dS} \tag{4}$$

and arises from the nonuniform production of Xe photoelectrons across the diameter of the optical cell due to focusing of the ArF beam. The integrals are taken over the cross-sectional surface area of the cylindrical waveguide, E_0 is the electric field amplitude expressed in terms of Bessel functions, and $f(\rho,\phi)$ describes the spatial dependence of the electron density. For a uniform electron distribution, $f(\rho,\phi)=1$. For the experimental arrangement described earlier, F was found to be $\frac{1}{150}$.

Remembering that the plasma frequency and electron density are related by the expressions

$$\omega_p^2=\frac{n_e e^2}{\epsilon_0 m}$$

or

$$\omega_p^2=3.18\times 10^9 n_e$$

(where n_e is in units of cm^{-3}), then the maximum photoelectron density existing along the axis of the Xe cell—*the peak electron density in both space and time*—can be determined from Eqs. (3) and (4) for a given ArF laser pulse energy.

B. Inclusion of excited-state photoelectrons

The situation is complicated by the second excimer pulse which photoionizes excited Xe molecules that are produced initially by the ArF pulse. Of course, the energy of the electrons produced by the second pulse depends on the laser's wavelength and the initial and terminal states involved in the ionizing optical transition. Therefore, immediately following the arrival of the latter laser beam at the cell, two groups of electrons are present—one with electron energies still very close to 0.7 eV and a second group having energies per electron of E_e. In order to calculate the electron density from the increased attenuation of the microwave signal, Eq. (3) is modified as follows:

$$\frac{F_2\omega_{p2}^2}{\nu_2^2+\omega^2}=\left[\frac{2\alpha^2c^2}{\nu_2^2}+\frac{F_1\omega_{p1}^2}{\nu_1^2+\omega^2}\frac{\nu_1}{\nu_2}\right]\left\{-1+\left[1+\left[\frac{\frac{4\alpha^2c^4}{\omega^2}(\alpha^2+\beta_g^2)-4\alpha^2c^2\frac{F_1\omega_{p1}^2}{\nu_1^2+\omega^2}-\nu_1^2\left[\frac{F_1\omega_{p1}^2}{\nu_1^2+\omega^2}\right]}{\left[\frac{2\alpha^2c^2}{\nu_2}+\frac{F_1\omega_{p1}^2}{\nu_1^2+\omega^2}\nu_1\right]^2}\right]^{1/2}\right]\right\}. \tag{5}$$

In this case, $\nu_1=3.3\times 10^{10}\ \mathrm{s}^{-1}$ for 0.7-eV electrons in 300 Torr of xenon, ν_2 is the collision frequency for electrons of energy E_e, ω_{p2} is their plasma frequency, ω_{p1} is the plasma frequency corresponding to the electron density existing immediately prior to the arrival of the second excimer laser pulse, and α is now the final (peak) attenuation coefficient, measured just after the second laser has fired. The instantaneous electron-density increase Δn_e due to the photoionization of Xe_2 excited states is calculated from Eq. (5) and the expression

$$\Delta n_e=\frac{\epsilon_0 m\omega_{p2}^2}{e^2}\ .$$

This analysis assumes that the original distribution of electron energies, essentially a δ function, remains fixed over the several hundred nanosecond time interval under consideration. Although this is a valid approximation during the second laser pulse ($\sim$25 ns wide at the 10% points) when the final attenuation measurement is made, it is expected that electron-electron collisions will tend to force the original electron energy distribution towards a Maxwellian.[27] An analytical solution to this problem has not yet been attempted but the effect of the electron-energy distribution on the final calculation of the electron density is expected to be small. Also, for convenience, F_2 is assumed to be equal to F_1.

It is obvious from (5) that Δn_e cannot be calculated unless the collision frequency ν_2 is known. From the values of σ_m tabulated by Frost and Phelps[28] and the known Xe density, the collision frequency is simply $\nu_m=[\mathrm{Xe}]\langle\sigma_m(E_e)v\rangle$ where the square brackets denote particle density (expressed in cm^{-3}) and the dependence of σ_m on E_e is shown explicitly. If the electron velocity v is assumed to be a constant rather than a distribution, then

$$\frac{\nu_2}{\nu_1}=\frac{\sigma_{m_2}v_2}{\sigma_{m_1}v_1}=\frac{\sigma_{m_2}}{\sigma_{m_1}}\left[\frac{E_2}{E_1}\right]^{1/2} \tag{6}$$

where the subscripts 1 and 2 are associated with the photoelectrons produced by the first and second laser pulses, respectively. Since ν_m was measured for 0.7-eV electrons, the collision frequency for any E_e is determined from Eq. (6) and existing cross-sectional data.

C. Sensitivity of the microwave detection system

For small values of microwave attenuation (α), Eq. (3) can be rewritten as

$$F\omega_p^2\approx 2\beta_g c^2\left[\frac{\nu_m^2+\omega^2}{\nu_m\omega}\right]\alpha\ , \tag{7}$$

and so n_e is directly proportional to α. The microwave detection of photoelectrons is most sensitive [i.e., right-hand side of (7) is minimized] when $\nu_m=\omega$. Therefore, since σ_m and ν_m are both dependent upon the ejected electron energy, there exists a value of E_e for which the detection system is most sensitive. As ν_m deviates from the value corresponding to this E_e, a larger "excess" electron density (Δn_e) is necessary to obtain a given attenuation of the microwave probe signal. Eventually, of course, the signal becomes undetectable or, more precisely, such electrons can be detected but the neutral molecular excited state associated with producing such energetic electrons would have to have a large photoionization cross section

(or population) indeed.

For the laser pulse energies and microwave diode used in these experiments, it was not possible to detect electrons with energies above ~ 2 eV. Therefore, using Eq. (6), it can be shown that the *lower* limit on the detectable electron energy is 0.02–0.04 eV. Consequently, we require $0.02 \leq E_e \lesssim 2$ eV.

Finally, the smallest attenuation that can be observed experimentally is $\alpha = 8.7 \times 10^{-4}$ cm^{-1} (which corresponds to a vertical deflection of approximately 1 mV on the storage oscilloscope). Consequently, for a given value of electron energy (and, hence, σ_m and ν_m), the minimum detectable concentration of electrons *having that energy* can be calculated from Eq. (3).

Figure 2 is a partial energy-level diagram of neutral and ionic Xe_2. The repulsive ground state of the dimer has been deleted for clarity. For reasons that will be described in detail in Sec. IV, one is forced to conclude that the Xe_2^* $0_u, 1_u$ and $1_g, 2_g$ states are responsible for the experimentally observed photoionization signal. Table I presents the electron energies and electron-neutral collisional data that are relevant to the photoionization of the lowest Xe_2 $0_u, 1_g$, and 2_g states. For all of the laser wavelengths shown (except KrF), photoionization of the $1_g, 2_g$ states is assumed. For a particular wavelength, Table I also lists the exiting electron energies (E_e) that would be expected for photoionization of the 0_u and $1_g, 2_g$ states. Although, for convenience, the Franck-Condon transitions are assumed to occur at the equilibrium radius for a given excimer state, the electron-density calculations are relatively insensitive to variations in E_e while the determination of the photoionization cross section is completely independent of E_e. Also shown in Table I are the momentum transfer cross sections of Frost and Phelps[28] and the collision frequency corresponding to that value of σ_m.

Considering the lowest 0_u^+ state of Xe_2^* and recalling the stipulation that $0.02 \leq E_e < 2$ eV, one concludes that the present system is useful for examining photoionization of the state at wavelengths from near the Xe_2^+ $1(\frac{3}{2})_g$ threshold ($\lambda \sim 264$ nm) down to at least 230 nm. Beyond this point, the $1(\frac{1}{2})_g$ state of Xe_2^+ is also accessible. Similarly, since the equilibrium radius R_e of the lowest 1_g and 2_g Xe_2^* states is approximately 7.0 a.u.,[29] these states can be studied via the $1_g, 2_g \rightarrow Xe_2^+$ $1(\frac{1}{2})_u$ transition for laser wavelengths in the spectral interval $300 \lesssim \lambda \lesssim 370$ nm while for the $1_g, 2_g \rightarrow Xe_2^+$ $1(\frac{3}{2})_u$ transition, $203 \lesssim \lambda \lesssim 318$ nm.

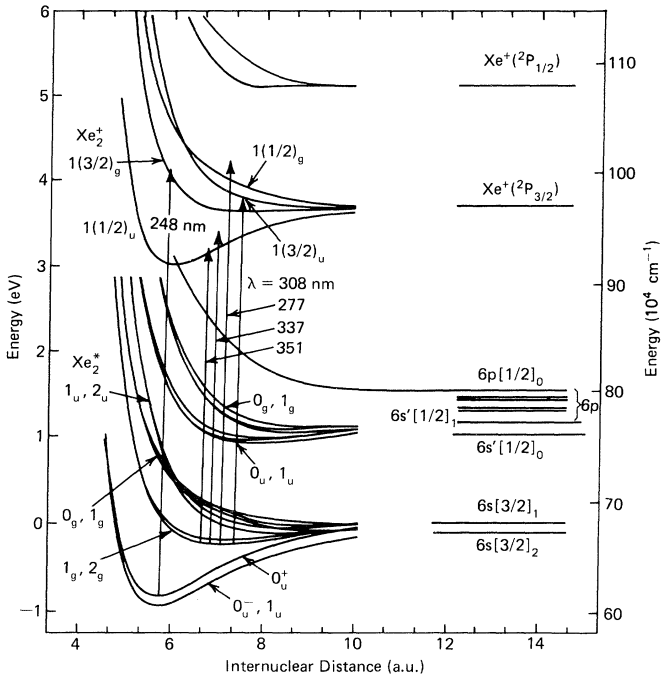

FIG. 2. Potential-energy curves for several of the lowest-lying Xe_2^* and Xe_2^+ molecular states (after Ermler *et al.*, Ref. 29). Photoionization of the lowest $0_u, 1_u$ and $1_g, 2_g$ levels of Xe_2 is also illustrated. The reasons for concluding that the molecular states indicated are those responsible for the photoionization signal will be discussed later in the text.

From the values of E_e for specific excimer laser wavelengths, the minimum detectable electron densities were calculated from Eq. (3) and the results are presented in the far right-hand column of Table I. For completeness, the pertinent data for the 0.7-eV electrons produced by two-photon ionization of $Xe(^1S_0)$ at 193 nm are presented at the bottom of the table.

In summary, the microwave system is sensitive over a sufficiently wide electron-energy range to allow for pho-

TABLE I. Electron energies and electron-neutral collisional data pertinent to photoionization of the 0_u, 1_g, and 2_g states of Xe_2^*.

Laser (wavelength in nm)		Exiting electron energy E_e (eV)	Transition	Cross section for momentum tranfer[a] σ_m (10^{-16} cm^2)	Electron-Xe collision frequency for $p_{Xe}=300$ Torr ν_m (10^{10} s^{-1})	Minimum detectable electron density (10^{11} cm^{-3})
XeF	(351.1)	0.1	$Xe_2^*(1_g,2_g) \rightarrow Xe_2^+$ $1(\frac{1}{2})_u$	20.0	18.5	3.8
N_2	(337.1)	0.25		5.4	7.9	2.3
XeCl	(307.9)	0.6		1.3	2.9	4.3
1st Stokes of KrF in H_2	(277.0)	1.05		2.7	8.1	4.1
		0.41	$1_g,2_g \rightarrow 1(\frac{3}{2})_u$	1.7	3.1	4.7
KrF	(248.4)	0.18	$0_u \rightarrow 1(\frac{3}{2})_g$	10.0	12.4	5.0
ArF	(193.3)	0.70	$Xe(^1S_0) \rightarrow Xe^+(^2P_{3/2})$	1.35	3.3	2.6

[a]Values are from Ref. 28.

toionization of the Xe_2^* 0_u and $1_g,2_g$ states to be examined over a large fraction of the ultraviolet region.

D. Determination of the photoionization cross section

The xenon dimer excited-state photoionization cross section σ_i is determined by simultaneously solving the kinetic rate equations which describe the temporal evolution of the excited-state population $[Xe_2^*]$ and Δn_e. Neglecting feeding and loss terms during the second laser pulse (12-ns FWHM, 25 ns at the 10% points), one finds that

$$\Delta n_e = N^*(1-e^{-\sigma_i E/\hbar\omega A}) \tag{8}$$

where N^* is the population (immediately prior to the arrival of the second laser pulse) of the molecular state being ionized and A is the cross-sectional area of the second laser beam at its focus. Therefore, a plot of Δn_e vs $E/\hbar\omega A$ (for a fixed time delay Δt—typically 300 ns—between the two lasers) should yield the exponential dependence described by (8) in which the saturated limit of the excess electron density is the population of the molecular state at that time. In order to determine the time evolution of the population of the excited state in question, the energy per pulse E of the second laser was held constant and Δn_e measured as Δt was changed from less than 100 ns to beyond 1 μs.

IV. EXPERIMENTAL RESULTS

A. Microwave attenuation (electron-density) waveforms

Figure 3 gives two examples of microwave attenuation oscillograms for 300 Torr of Xe partially ionized initially by ArF radiation, followed $\sim$300 ns later by an N_2 laser pulse. The ArF and N_2 laser focal intensities for the two photographs are (a) $I_{ArF}=90$ MW cm^{-2} and $I_{N_2}=12$ MW cm^{-2}, (b) $I_{ArF}=100$ MW cm^{-2} and $I_{N_2}=16$ MW cm^{-2}. Also, attenuation (and, therefore, electron density) increases vertically as shown. The baseline (lowest horizontal line on the graticule) indicates the position of the dc microwave signal and a silicon detector was calibrated with a precision attenuator to determine the attenuation necessary to produce a given deflection from the baseline. The waveforms shown in Fig. 3 are similar to one first reported in Ref. 24.

Figure 3(a) shows the entire electron-density waveform while 3(b) gives only the latter portion of the signal so as to accentuate the excess electron density (i.e., beyond the ArF laser-produced "background") produced by the N_2 laser. Actually, two waveforms are superimposed in 3(b). One shows the observed temporal history of the electron density when only the 193-nm optical field is present while the second illustrates the difference when both lasers are fired (same ArF intensity). Two points can be made about each of the three waveforms. The reproducibility of the traces was excellent for all of the data taken (better than 5%). Secondly, an instantaneous increase in the electron density is clearly evident when the N_2 pulse arrives at the cell. At this point it should be mentioned that detailed measurements were made to verify that waveforms such as those in Fig. 3 were due to absorption

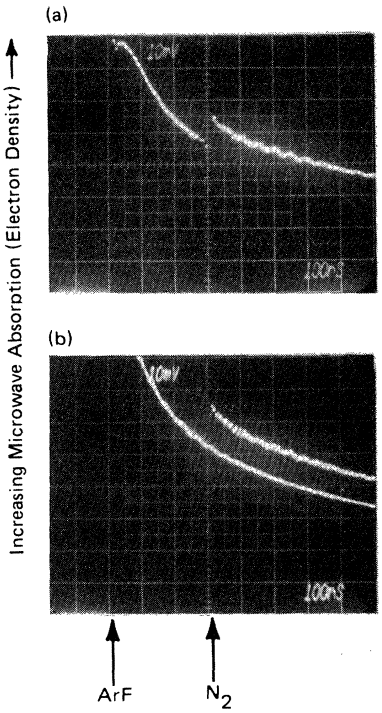

FIG. 3. Typical microwave-absorption oscillograms for 300 Torr of Xe irradiated initially by ArF (193 nm) followed $\sim$300 ns later by an N_2-laser (337 nm) pulse. Photograph (a) shows the entire waveform and two waveforms are superimposed in (b)—one showing the effect of both laser pulses and a second associated with only the 193-nm beam. Microwave absorption (and, hence, electron density) increases vertically. The ArF pulse produces a peak electron density of $\sim 2.4\times10^{13}$ cm^{-3} and 3.0×10^{13} cm^{-3} for (a) and (b), respectively, and the N_2 laser radiation leads to an instantaneous jump in the electron density. The ArF and N_2 laser intensities are 90 and 12 MW cm^{-2}, respectively, in (a) and 100 and 16 MW cm^{-2} ($E_{N_2}\cong 10$ mJ, $\Phi_{N_2}=E_{N_2}(\hbar\omega A)^{-1}=2.2\times10^{17}$ cm^{-2}) in (b).

of the microwave probe rather than reflection of power back towards the klystron. Note that the vertical axes in Figs. 3(a) and 3(b) are not linear in electron density. In 3(a), for example, the vertical deflection sensitivity is 10 mV per large division and so at 10 mV above the baseline (bottom of graticule), the detection system sensitivity is 2.64×10^{11} cm^{-3}(mV)$^{-1}$. At the top of the oscillogram (80 mV), the resolution has fallen to 2.80×10^{11} cm^{-3}(mV)$^{-1}$.

When the ArF laser is fired, absorption of the microwave probe signal in 3(a) rises rapidly to a peak absorption of 32% at the end of the pump pulse ($\sim$15–20 ns), signifying the presence of a large ($>2\times10^{13}$ cm^{-3}) electron density produced by two-photon ionization of Xe at 193 nm. These initial electrons decay by dissociative recombination of Xe_2^+ and the electron density is 1.45×10^{13} cm^{-3} when a nitrogen laser is fired at $\Delta t=300$ ns. The N_2 laser pulse ionizes (as will be shown later) excited xenon dimers, thereby increasing the electron density by 2.9×10^{12} cm^{-3}. For all of the experimental data to be described later, the ArF laser pulse energy and the timing between the two lasers (300 ns) were

fixed such that the background electron density was 1.65×10^{13} cm^{-3} [corresponding to a 60-mV deflection from the baseline as shown in Fig. 3(b)] just prior to the second laser pulse. The total deflection gave the final attenuation α, which was substituted into Eq. (5).

B. Temporal history of the state(s) being ionized

The first step towards determining the identity of the state being photoionized is to measure the variation of its *relative* population with time. As mentioned previously, this was accomplished by measuring the *unsaturated* Δn_e (since only relative values are needed) for various time delays between the two excimer laser pulses with the intensities of each laser held constant. As shown in Fig. 4 for $\lambda=307.9$ nm and the ArF and XeCl focal laser intensities fixed at 80 and 25 MW cm^{-2}, respectively, Δn_e peaks $\sim$400 ns after the ArF laser is fired. Since N* is proportional to Δn_e [Eq. (8)], we conclude that the population of the as yet unidentified species also reaches maximum for $\Delta t=400$ ns. As also illustrated in the figure, an almost identical result was obtained for $\lambda=351.1$ nm (XeF laser, $I_{\mathrm{XeF}}=50$ MW cm^{-2}). Higher ArF intensities cause N^* to peak earlier in time as is borne out by the data of Fig. 6, Ref. 24. In that case, $I_{\mathrm{ArF}}=112$ MW cm^{-2} which gives an electron density that is 71% larger[25] than that at 80 MW cm^{-2}. Therefore, since the recombination rate for Xe_2^+ ions is proportional to n_e, the Xe excited-state densities, and hence the Xe_2^* population, build up much more rapidly for the larger ArF intensities. With I_{ArF} held constant, however, the variation of Δn_e (N*) with time is (to within experimental error) the same at these two wavelengths.

C. Laser-induced fluorescence and spontaneous emission measurements of excited-state temporal histories

It was stated in Sec. III C that photoionization of certain Xe_2^* states accounts for the excess electron production

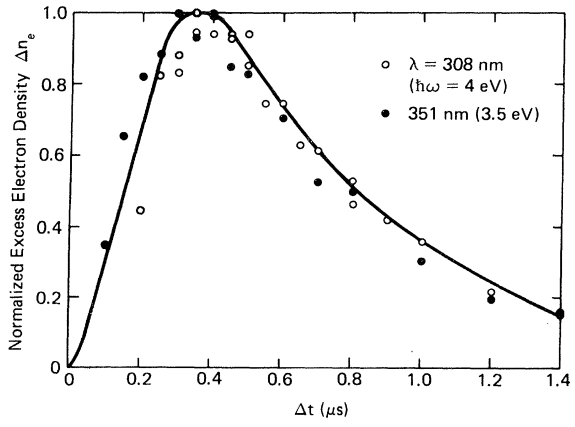

FIG. 4. Temporal variation of the number density of the unknown species for photoionization at 308 and 351 nm. The ArF, XeF, and XeCl laser intensities were fixed at 80, 50, and 30 MW cm^{-2}, respectively, and Δt is the time delay between the two lasers (ArF laser fired first at $t=0$).

that was described earlier, and the experimentally measured time required for N* to peak seems to buttress this argument. However, a convincing identification of the atomic or molecular state(s) responsible requires that comparison be made between the temporal history of known levels that might reasonably be involved and that for the unidentified species. Consequently, a series of laser-induced fluorescence and spontaneous emission experiments, designed to examine the histories of various Xe atomic excited states, were conducted with the apparatus illustrated schematically in Fig. 5. Atomic states were chosen for study simply because their energy levels are much better known than are those for the dimer.

The excited states of Xe were produced indirectly by two-photon ionization of Xe at 193 nm (Ref. 25) (ArF excimer laser) followed by dissociative recombination of Xe_2^+. As was done earlier, the Xe cell was irradiated transversely, producing a linear excitation region $\sim$3 cm in length.

The temporal histories of every $6p$ state: $6p[\frac{1}{2}]_0$, $6p[\frac{3}{2}]_2$, $6p[\frac{5}{2}]_3$, $6p[\frac{3}{2}]_1$, $6p[\frac{5}{2}]_2$, and $6p[\frac{1}{2}]_1$, as well as the $6p'[\frac{3}{2}]_2$ level were studied in emission by viewing the axis of the Xe cell with a 0.6-m Hilger-Engis spectrograph (0.14-nm/mm resolution in first order) and an RCA 7102 (S-1) photomultiplier.

The transitions examined were $6p[\frac{1}{2}]_0\rightarrow6s[\frac{3}{2}]_1$ (828.0 nm), $6p[\frac{3}{2}]_2\rightarrow6s[\frac{3}{2}]_2$ (823.2 nm), $6p[\frac{5}{2}]_3\rightarrow6s[\frac{3}{2}]_2$ (881.9 nm), $6p[\frac{3}{2}]_1\rightarrow6s[\frac{3}{2}]_1$ (916.3 nm), $6p[\frac{5}{2}]_2\rightarrow6s[\frac{3}{2}]_2$ (904.5 nm), $6p[\frac{1}{2}]_1\rightarrow6s[\frac{3}{2}]_2$ (980.0 nm), and $6p'[\frac{3}{2}]_2\rightarrow6s'[\frac{1}{2}]_1$ (834.7 nm). Owing to the weak spontaneous emission signals involved, the fluorescence waveforms were recovered using a Princeton Applied Research 162 boxcar integrator with a 10-ns-wide gate and a strip-chart recorder. To within experimental error, *all* of the transitions studied behave in a nearly identical manner, exhibiting peak fluorescence $\sim$100 ns following the firing of the ArF laser. The e^{-1} decay time for the waveforms is typically 250–350 ns. As far as signal amplitudes are concerned, the $6p[\frac{1}{2}]_0\rightarrow6s[\frac{3}{2}]_1$ emission at 828 nm was considerably stronger than the others. From the transition branching ratios measured by Horiguchi *et al.*[30] for various $6p$ states of Xe, calculations of the relative peak populations of the $6p$ states were made and the results are given in Table II where the states are ranked in descending order according to their energies. The temporal histories of the $6p[\frac{1}{2}]_1$ and $6p[\frac{3}{2}]_2$ states were also measured by LIF experiments on the $6p[\frac{3}{2}]_2\rightarrow7d[\frac{5}{2}]_3$ (739.4 nm) and $6p[\frac{1}{2}]_1\rightarrow8s[\frac{3}{2}]_1$ (738.6 nm) transitions and the results corroborated the emission studies.

In order to study the Xe $6s$ and $6s'$ states, the vacuum-ultraviolet wavelengths of the $6s[\frac{3}{2}]_1\rightarrow{}^1S_0$ (147.0 nm) and $6s'[\frac{1}{2}]_1\rightarrow{}^1S_0$ (129.6 nm) resonance lines made it necessary to again resort to LIF. For these experiments, a pulsed, excimer-pumped dye laser (10-ns FWHM pulses, $\Delta\lambda\lesssim10^{-2}$ nm or 0.2 cm^{-1} except for $\lambda\gtrsim700$ nm where $\Delta\lambda\sim0.1$ nm) was tuned to one of three transitions: $6s[\frac{3}{2}]_1\rightarrow6p'[\frac{3}{2}]_1$ at 491.7 nm, $6s[\frac{3}{2}]_1\rightarrow7p[\frac{1}{2}]_0$ at 480.7 nm or $6s'[\frac{1}{2}]_1\rightarrow4f[\frac{3}{2}]_2$ at 732.1 nm. To ensure that the dye laser was tuned to the correct wavelength, the beam was passed through a low pressure (0.5 Torr) Xe discharge

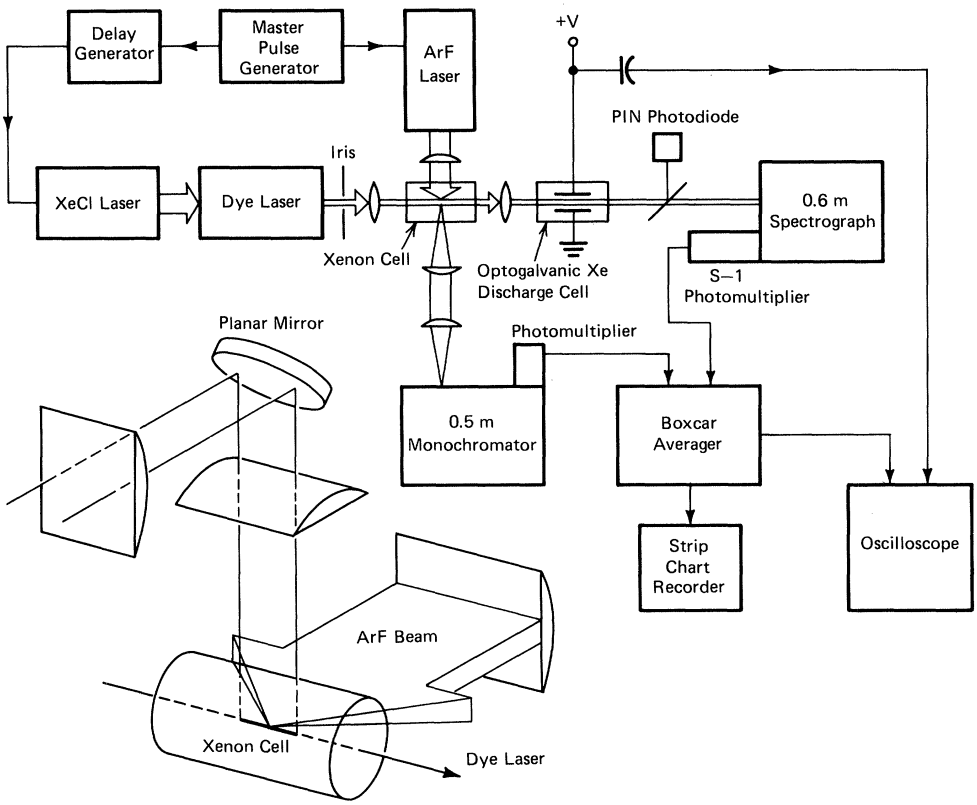

FIG. 5. Experimental setup for the measurement of the time behavior of several Xe $6p$, $6p'$, $6s'$, and $6s$ atomic-state populations by LIF or spontaneous emission. The inset is a more detailed diagram of the collection optics and geometry for the detection system.

and resonance observed by means of the optogalvanic effect.

The dye laser beam was directed along the axis of the Xe tube such that it was colinear with the focus of the ArF beam and a digital delay generator again controlled the relative timing between the two laser pulses. The LIF was collected and imaged onto the slits of a 0.5-m Jarrell-Ash monochromator with a simple telescope ($f/4$ optics) consisting of cylindrical lenses and an aluminized planar mirror (see inset, Fig. 5). Because of the shorter wavelengths involved, an RCA C31034A (GaAs photocathode) photomultiplier was used and the temporal history of the LIF again obtained with a boxcar and strip-chart recorder. Alignment of the detection system, which was found to be crucial, consisted of replacing the Xe cell with a tungsten ribbon lamp and mounting the lamp so that the filament lay horizontally and at the intersection of the dye and excimer laser beams. The luminous region of the filament was then imaged onto the slits of the monochromator using the lenses and mirror. To optimize the system's collection efficiency, the monochromator was placed on its side so that the slits and filament image were parallel.

For each of the dye laser transitions mentioned above, the resulting LIF was, for convenience, monitored on the

TABLE II. Relative populations of the $6p$ levels of Xe.

State	Transition examined	Relative emission intensity	Transition branching ratio[a]	Relative peak population[b]
$6p'[\frac{3}{2}]_2$	$6p'[\frac{3}{2}]_2 \rightarrow 6s'[\frac{1}{2}]_1$ (834.7 nm)	0.1	0.733	0.08
$6p[\frac{1}{2}]_0$	$6p[\frac{1}{2}]_0 \rightarrow 6s[\frac{3}{2}]_1$ (828.0 nm)	8.9	0.998	4.5
$6p[\frac{3}{2}]_2$	$6p[\frac{3}{2}]_2 \rightarrow 6s[\frac{3}{2}]_2$ (823.2 nm)	2.1	0.7	1.5
$6p[\frac{3}{2}]_1$	$6p[\frac{3}{2}]_1 \rightarrow 6s[\frac{3}{2}]_1$ (916.3 nm)	1.2	0.915	1.0
$6p[\frac{5}{2}]_3$	$6p[\frac{5}{2}]_3 \rightarrow 6s[\frac{3}{2}]_2$ (881.9 nm)	5.3	1.0	3.2
$6p[\frac{5}{2}]_2$	$6p[\frac{5}{2}]_2 \rightarrow 6s[\frac{3}{2}]_2$ (904.5 nm)	1.0	0.363	1.9
$6p[\frac{1}{2}]_1$	$6p[\frac{1}{2}]_1 \rightarrow 6s[\frac{3}{2}]_2$ (980.0 nm)	1.1	0.917	1.5

[a]Values are from Horiguchi *et al.*, Ref. 30.

[b]The relative peak population is defined as the relative intensity divided by the product of the detector response at that wavelength and the branching ratio.

$6p[\frac{1}{2}]_0 \rightarrow 6s[\frac{3}{2}]_1$ transition at 828.0 nm. Figure 6 shows that, due to the large quenching rates and short radiative lifetimes for the Xe np and np' levels,[26,30] this approach only slightly distorts the true temporal dependence of the initial-state's population. A partial energy-level diagram for atomic xenon is given in Fig. 6(a) and the transitions used to probe the resonant $6s[\frac{3}{2}]_1$ state ($^3P_1$ and $1s_4$ in LS coupling and Racah notation, respectively) are also indicated. The $6p \rightarrow 6s$ LIF waveform at 828 nm that results from pumping the $6s[\frac{3}{2}]_1 \rightarrow 7p[\frac{1}{2}]_0$ Xe transition with a dye laser is compared to the actual dye-laser pulse in Fig. 6(b). Despite the "two-step" process by which $7p[\frac{1}{2}]_0$ atoms return to the initial $6s[\frac{3}{2}]_1$ level, the dye-laser pulse width is stretched by only 14 ns. Therefore, relaxation of the $7p[\frac{1}{2}]_0$ and $6p'[\frac{3}{2}]_1$ states to the $6p[\frac{1}{2}]_0$ level is so rapid at these pressures (300 Torr Xe) that monitoring the $6p[\frac{1}{2}]_0 \rightarrow 6s[\frac{3}{2}]_1$ line is essentially equivalent to looking directly at the upper state of the dye-laser–pumped transition. Similar comments hold for the $6s'[\frac{1}{2}]_1 \rightarrow 4f[\frac{3}{2}]_2$ transition which has not been included in Fig. 6.

The results of the LIF and $6p$ spontaneous emission experiments are summarized in Fig. 7 which shows a representative Xe $6p \rightarrow 6s$ fluorescence waveform and the temporal histories of the Xe $6s[\frac{3}{2}]_1$ and $6s'[\frac{1}{2}]_1$ states as determined by LIF. For convenience, the variation of N* with time (from Fig. 4) is also shown. Owing to the weakness of the LIF signal, it was not possible to monitor the $6s'$ concentration for $\Delta t < 300$ ns. However, as pointed out by several groups,[31–33] the proximity of the $6s'[\frac{1}{2}]_1$ state to the $6p[\frac{1}{2}]_1$ level leads to strong collisional coupling between the two. Consequently, as confirmed by the partial results in Fig. 7, Sadeghi and Sabbagh[33] have shown that the temporal histories of the two states are nearly identical, even for xenon pressures as low as 0.06 Torr.

Clearly, none of the atomic states studied even roughly matches the time behavior of the population of the species in question and are therefore unable to account for the observed photoionization. Hence, we are forced to conclude that a molecule, not an atomic excited state, is the responsible species. A simple calculation demonstrates that this is a plausible conclusion. If one somewhat arbitrarily associates N* with a molecular state arising from Xe $6s[\frac{3}{2}]_1$ and $^1S_0$ atoms and assuming that the Xe $6s[\frac{3}{2}]_1$ population decays almost exponentially for $t > 200$ ns,

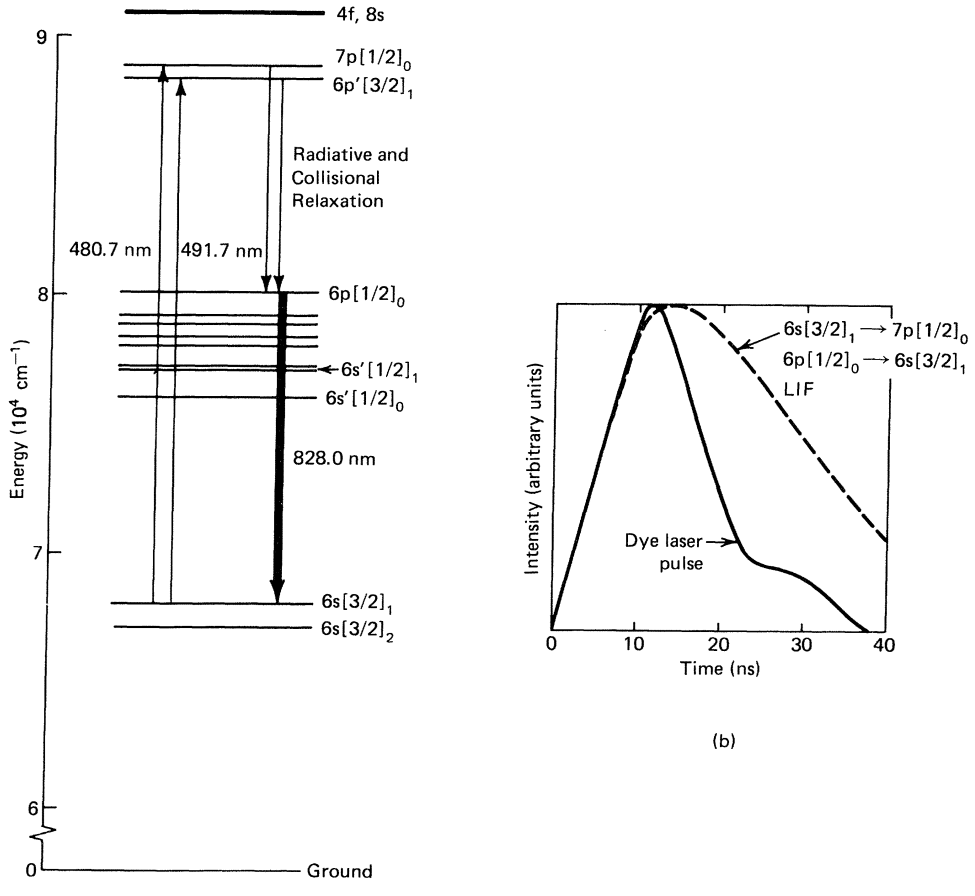

FIG. 6. (a) Partial energy-level diagram for atomic Xe showing states relevant to the detection of Xe $6s[\frac{3}{2}]_1$ atoms by LIF. (b) demonstrates that monitoring the $6p \rightarrow 6s$ line at 828.0 nm, rather than looking directly at a transition originating from the $7p[\frac{1}{2}]_0$ or $6p'[\frac{3}{2}]_1$ states, distorts the true dye laser waveform by ~ 14 ns which is negligible compared to the lifetime of the $6s[\frac{3}{2}]_1$ population (FWHM is approximately 250–300 ns). Similar data and comments hold for the other $6p$ and $6s'$ states which were studied by LIF.

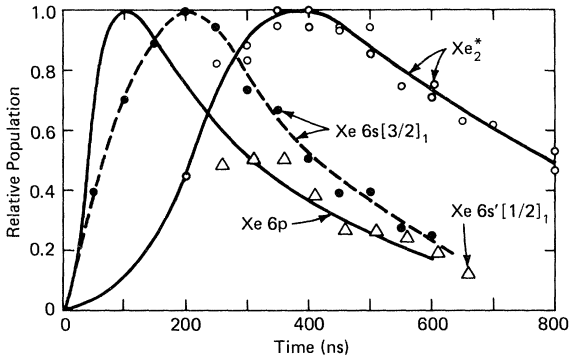

FIG. 7. Comparison of the temporal histories of the populations of selected Xe $6s$, $6s'$, and $6p$ levels. All of the $6p$ states ($[\frac{1}{2}]_0$, $[\frac{3}{2}]_2$, $[\frac{5}{2}]_3$, $[\frac{3}{2}]_1$, $[\frac{5}{2}]_2$, $[\frac{1}{2}]_1$) and the $6p'[\frac{3}{2}]_2$ level are represented by a single waveform since their temporal behavior is identical to within experimental error. The molecular profile was taken from Fig. 4 ($\lambda=308$ nm) and is very similar to Fig. 6 of Ref. 24 in which $\lambda=351.1$. In this case, the photoionization wavelength is 307.9 nm. As noted in the text, accurately monitoring the $6s'[\frac{1}{2}]_1$ population was only possible for delay times $\gtrsim$250–300 ns. Also note that the molecular species curve peaks much later in time than any of the atomic-state number densities. For all of the data shown, $80 \leq I_{\mathrm{ArF}} \leq 90$ MW cm^{-2}.

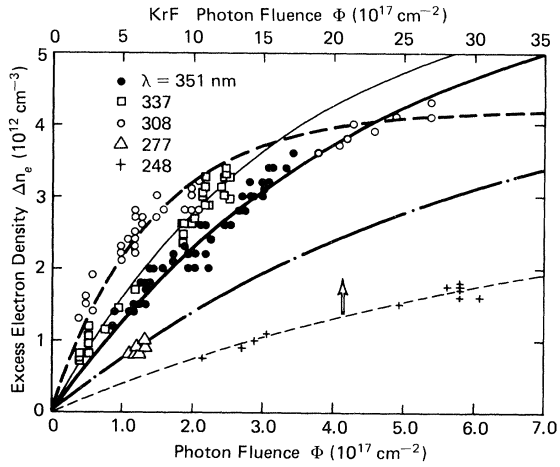

FIG. 8. Instantaneous excess electron density Δn_e (beyond the background density produced solely by the ArF laser) as a function of the photon flux from the second (ionizing) laser pulse. For the data, $I_{\mathrm{ArF}}=100$ MW cm^{-2} and $\Delta t=300$ ns. The saturated limits for the 351-, 337-, 308-, and 277-nm data lie between 4.2×10^{12} and 6.3×10^{12} cm^{-3} while at 248 nm, the saturated Δn_e is 3.2×10^{12} cm^{-3}. The 351-nm data are nearly identical to that shown in Fig. 5 of Ref. 24. The curves shown represent computer fits of the data to Eq. (14).

then the time rate of change of the Xe* and Xe_2^* populations can be expressed in rate equation form as

$$\frac{d[\mathrm{Xe}^*]}{dt'} = -k_f[\mathrm{Xe}]^2[\mathrm{Xe}^*] \tag{9}$$

and

$$\frac{d[\mathrm{Xe}_2^*]}{dt'} = +k_f[\mathrm{Xe}]^2[\mathrm{Xe}^*] - \frac{[\mathrm{Xe}_2^*]}{\tau} , \tag{10}$$

where $t'=0$ is defined to be at the peak of the $6s[\frac{3}{2}]_1$ curve, k_f is the three-body formation rate constant (expressed in cm^{6}s^{-1}) for the Xe_2^* species, τ is the effective lifetime of the Xe_2^* states, and excimer molecule formation is assumed to be the dominant loss process for $6s[\frac{3}{2}]_1$ atoms at this pressure (300 Torr; resonance radiation trapping greatly extends the $6s[\frac{3}{2}]_1 \rightarrow {}^1S_0$ spontaneous emission lifetime).

Consequently,

$$[\mathrm{Xe}^*] = Ae^{-Bt'} \tag{11}$$

and

$$\frac{d[\mathrm{Xe}_2^*]}{dt} + \frac{[\mathrm{Xe}_2^*]}{\tau} = ABe^{-Bt'} ,$$

where

$$B = k_f[\mathrm{Xe}]^2 \tag{12}$$

and A is the peak ($t'=0$) Xe* number density. Therefore,

$$[\mathrm{Xe}_2^*] = \left[\frac{AB}{B-1/\tau}\right](e^{-t'/\tau} - e^{-Bt'}) . \tag{13}$$

Then, if $B \gg 1/\tau$, $k_f[\mathrm{Xe}]^2$ is associated with the leading edge of the N* temporal profile.

Subsequently, from Fig. 7

$$k_f[\mathrm{Xe}]^2 \approx (200\ \mathrm{ns})^{-1}$$

or

$$k_f \approx 5\times10^{-32}\ \mathrm{cm}^6\mathrm{s}^{-1}$$

for $[\mathrm{Xe}]=9.6\times10^{18}$ cm^{-3}. This value is almost precisely that expected from those already existing in the literature.[34]

In summary, detailed studies of the temporal history of the populations of *every* Xe($6p$) state as well as the $6s'[\frac{1}{2}]_1$ and $6s[\frac{3}{2}]_1$ levels lead to the conclusion that these species are not those responsible for the observed photoionization signal. On the contrary, the time dependence of N* points to a molecular (Xe_2) level.

D. Photoelectron density data

Figure 8 presents the results of measurements of the peak (initial) electron density increase as a function of the photon fluence [$\Phi=(\hbar\omega A)^{-1}E_{\mathrm{laser}}$, A is the beam cross-sectional area] of the second laser for five wavelengths between 248 and 351 nm. Acquiring the data consisted of recording the total microwave signal deflection from the baseline while varying the ionizing laser pulse energy. The attenuation was then calculated for each pulse, and the measurements were repeated for each laser wavelength studied. The 351-nm data is essentially equivalent to that shown in Fig. 5 of Ref. 24. Note that the photon fluence scale for $\lambda=248$ nm is different from that for the other wavelengths simply because the electron densities mea-

sured for photoionization at the KrF laser wavelength were so much smaller than those observed elsewhere.

For each wavelength, the best fit of the equation

$$\Delta n_e(\Phi)=C(1-e^{-D\Phi}) \tag{14}$$

(where Φ is again the laser photon fluence) to the data was calculated by a computer. Of course, (14) is a modified expression for Eq. (8) in which the constant C represents the *saturated* excess electron density and is equal to N^*, the number density of the Xe_2 excited state being ionized. D, on the other hand, is the photoionization cross section of the state at the wavelength under consideration.

For $\lambda=351$, 308, 337, and 277 nm, the saturated electron-density values (C) (measured 300 ns after the ArF pulse) were found to be 6.3×10^{12}, 4.2×10^{12}, 6.1×10^{12} and 5.0×10^{12} cm^{-3}, respectively. Although the laser energies available at 277 nm were such that Δn_e could not be saturated, the flux range studied was sufficiently large that it is concluded that the 277-nm saturation limit is correct to within 20% [$(5\pm1)\times10^{12}$ cm^{-3}]. At 351, 308, and 337 nm, the uncertainty in $(\Delta n_e)_{SAT}$ is less since, as can be seen from Fig. 8, measurements of Δn_e at 308 nm nearly reach the saturated limit for $\Phi_{XeCl}>2\times10^{17}$ cm^{-2} while at 337 and 351 nm, excess electron densities more than 56% and 57%, respectively, of the computed saturation limit were recorded. Consequently, the uncertainties in the saturated electron densities at 308, 337, and 351 nm are estimated to be $\pm10\%$ at 351 and 337 nm and $\pm15\%$ at 308 nm. These errors represent 1 standard deviation in the saturated values of Δn_e that were determined by the computer from the data. The results suggest that the same excited state is being photoionized at the four wavelengths between 277 and 351 nm. At 248 nm, the saturated Δn_e predicted by the data (3.2×10^{12} cm^{-3}) is significantly smaller than for the other wavelengths and this is reinforced by the much smaller cross section observed with the KrF laser. Therefore, it appears that a different initial state is involved for $\lambda=248$ nm.

E. Measured photoionization cross sections

The measured photoionization cross sections (determined from the data of Fig. 8) are listed in Table III and plotted in Fig. 9. A peak value of $\sim7\times10^{-18}$ cm^2 occurs for $\lambda=308$ nm (XeCl laser) but the cross section falls rapidly for shorter wavelengths. One of the major sources of error in the $\lambda=248$-nm cross section is the rising importance of two-photon excitation of the Xe $6p[\frac{1}{2}]_0$ state at 80 119 cm^{-1} for KrF laser pulse energies $\gtrsim100$ mJ. Indirect feeding of the $6s$ and $6s'$ atomic states results, culminating in additional production of excited dimers. This complicates the analysis of the data since an increase in $[Xe_2^*]$ also leads to a rise in the dimer ionization rate. This complication is reflected by the larger error bars for the 248-nm datum. As indicated in Fig. 9, the uncertainty in the cross sections is $\pm10\%$ for $\lambda=277$, 337, and 351 nm, $\pm15\%$ at 308 nm, and $\pm20\%$ at 248 nm. Again, the error in the cross sections is 1 standard deviation and arises primarily from the uncertainty associated with calibration of the photodiodes used in laser intensity measurements. The electron-density measurements themselves are not a major source of error—the microwave "attenuation" waveforms are nearly noise-free and the only errors from this aspect of the studies stem from the estimated 5% uncertainty in reading the peak attenuation from an oscilloscope display.

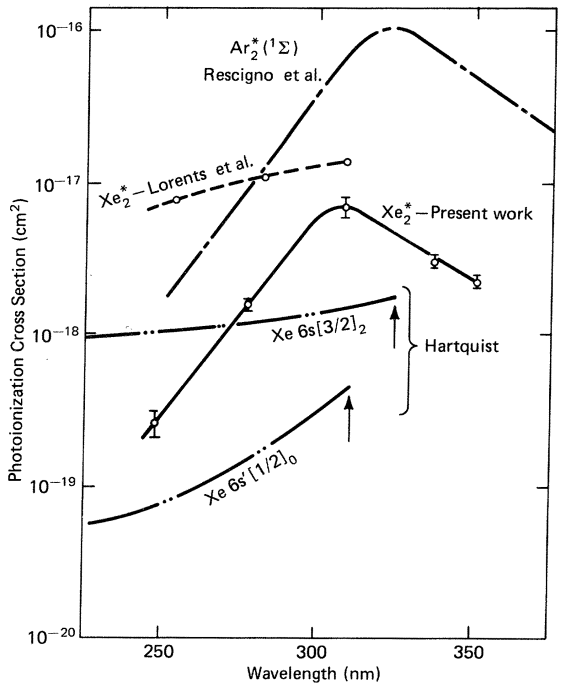

FIG. 9. Measured Xe_2^* photoionization cross sections for several different ultraviolet laser wavelengths. These are compared with theoretical values calculated by Lorents *et al.* (Ref. 22) for Xe_2^* and the calculations of Rescigno *et al.* (Ref. 23) for the $^1\Sigma$ state of Ar_2^*. The photoionization profiles reported by Hartquist (Ref. 16) for the Xe $6s[\frac{3}{2}]_2$ and $6s'[\frac{1}{2}]_0$ atomic states are also shown.

TABLE III. Photoionization cross sections measured for excited states of molecular xenon.

Molecular state(s)	Wavelength (nm)	Ionization cross section σ_i (10^{-18} cm^2)	Saturated electron density $(\Delta n_e)_{I\to\infty}=N^*$ (10^{12} cm^{-3})
$Xe_2^*(1_g,2_g)$	351.1	2.3	6.3
	337.1	3.0	6.1
	307.9	7.1	4.2
	277.0	1.6	5.0
$Xe_2^*(0_u)$	248.4	0.26	3.2

The results for XeF (351 nm) also illustrate the insensitivity of the cross-section measurement to the value chosen for E_e. In an earlier paper in which the photoionization effect was first reported,[24] photoionization of a $6s'$ atomic state was assumed to be responsible which gave an E_e of ~0.85 eV. However, after identifying Xe_2^* as the species in question, the ejected electron energy is only ~0.1 eV and yet the cross sections measured in each case are identical (2.3×10^{-18} cm^2) to less than 5%. The ma-

jor change involves N^* which increases from 5×10^{12} cm^{-3} to 6.3×10^{12} cm^{-3} in the present case—still not a serious deviation. Consequently, one very attractive aspect of this approach to measuring photoionization cross sections is that it is virtually independent of the precise shape of the molecular state potential curves.

V. DISCUSSION

A. Kinetics

The optical and kinetic sequence by which Xe_2 excited states are produced and subsequently ionized is depicted in Fig. 10. Xenon ions in the $^2P_{3/2}$ configuration are initially produced from ground-state atoms by the simultaneous absorption of two 193.3-nm ($\hbar\omega=6.4$ eV) photons.[25] A 0.7-eV electron is also produced by this process and for the Xe pressures used in these experiments (300 Torr), cooling of the photoelectrons by elastic electron-neutral collisions is slow [electron temperature (T_e) relaxation time is approximately 3 μs (Ref. 27)]. Consequently, T_e is assumed to be constant over the time scale of these experiments.

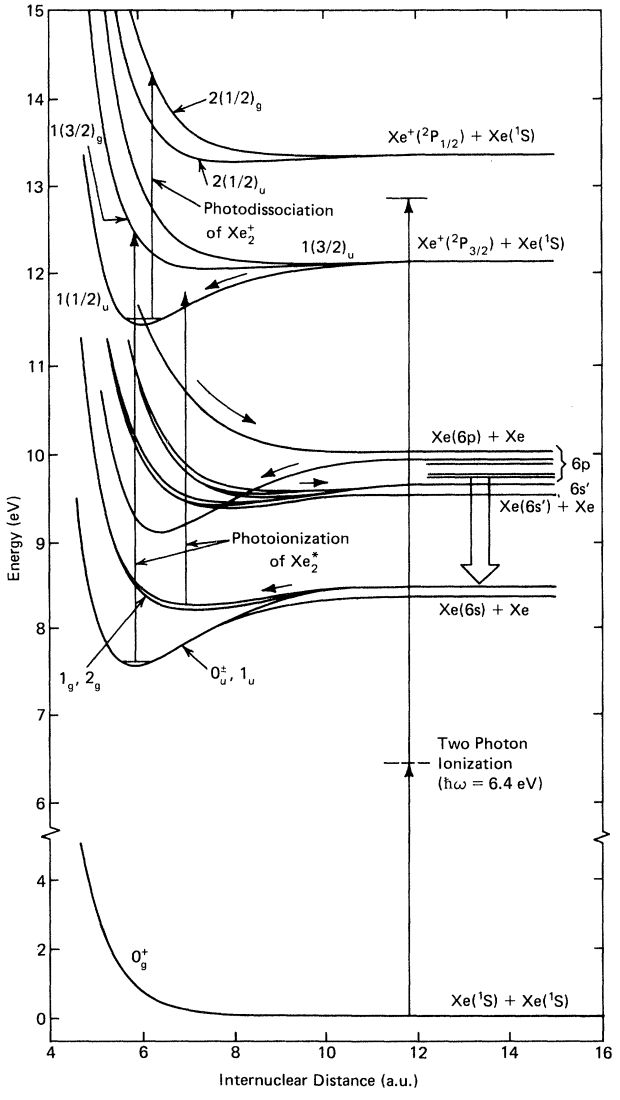

FIG. 10. Generalized energy-level diagram for Xe_2^* and Xe_2^+ illustrating the optical and collisional processes that dominate the kinetics of these experiments. Soon after Xe^+ ($^2P_{3/2}$) ions are produced by two-photon ionization ($\hbar\omega=6.4$ eV) of Xe ($^1S_0$), Xe_2^+ ions are formed and are subsequently lost to dissociative recombination. The Xe $6p$ manifold relaxes collisionally, radiatively, and by dissociation of higher-lying, unstable Xe_2 excited states. Photodissociation of Xe_2^+ on the $1(\frac{1}{2})_u \rightarrow 2(\frac{1}{2})_g$ transition is also shown.

Dimerization of the $Xe^+(^2P_{3/2})$ species to form Xe_2^+ molecular ions in the ground $[1(\frac{1}{2})_u]$ state is rapid (τ^{-1} at 300 Torr Xe $\simeq 2\times10^7$ s^{-1}). As shown in the figure, the Xe ($6p$) manifold of states ($6p[\frac{1}{2}]_0$, $6p[\frac{3}{2}]_2$, and $6p[\frac{5}{2}]_3$, in particular) is known to be strongly fed by dissociative recombination of Xe_2^+ with the "hot" (0.7 eV) electrons.[35] Collisional relaxation of the $6p$ manifold is rapid[26,30] and so lower-lying $6p$, $6s'$, and $6s$ levels are quickly populated.

At this point, it should be emphasized that, as indicated in Fig. 10, the $6p$ states relax to the $6s$ and $6s'$ levels by several channels. Of course, spontaneous emission is strong due to the 30—40-ns radiative lifetimes of the individual states[30] and the two-body quenching-rate constants are also large—within an order-of-magnitude of gas kinetic.[30] In addition, as noted by Mulliken[36] in his classic paper on the excited-state structure of Xe_2, although the $6p$ atomic states do form strongly-bound $1_u,0_u^-$ and $1_g,0_g^-$ molecular levels, these states are unstable with respect to dissociation or predissociation since they are crossed by repulsive curves associated with the $Xe^*(6s')+Xe$ asymptote.[33,36] Consequently, molecular formation followed rapidly by dissociation of the species is a viable loss channel for $6p$ atoms.[33]

Once formed, Xe $6s$ atoms are subsequently able to populate low-lying Xe_2 excited states through a three-body collision with two background $^1S_0$ atoms. A uv pulse from a second laser (XeF: 351.1 nm; N_2: 337.1 nm; XeCl: 307.9 nm; KrF: 248.4 nm, or KrF Raman shifted in H_2: 277.0 nm) subsequently ionizes molecules in those energy levels. Of course, the photoelectron density is dominated by those Xe_2 excited states that have substantial populations *and* large photoionization cross sections. Guaranteeing that predominantly Xe_2 excimers, rather than atomic excited states, are photoionized is accomplished by exploiting Fig. 7—namely, simply delaying the second laser pulse until the Xe_2^+ $1(\frac{1}{2})_u$ and $Xe^*(6s,6s'$, and $6p)$ number densities fall below their peak values.

Further proof that the Xe_2 dimer is being photoionized in these experiments rests on remembering that the same uv radiation that photoionizes Xe_2^* is also capable of photodissociating Xe_2^+ (cf. Ref. 24). To this point, the discussion has centered on the temporal and laser intensity dependence of the electron density as deduced from microwave-absorption measurements. However, the Xe $6p\rightarrow6s$ fluorescence has been shown[24] to accurately reflect the Xe_2^+ $1(\frac{1}{2})_u$ number density. Consequently, the depletion of the Xe_2^+ ground-state population by uv photodissociation manifests itself as a strong suppression in the emission from the Xe $6p$ states.

If, as indicated in Fig. 10, the Xe_2^+ population is bolstered by Xe dimer photoionization at the same time as

photodissociation reduces its density, the competition between the two processes should be observable from Xe* spontaneous emission waveforms. Specifically, the time rate of change of the Xe_2^+ population can be written [by modifying Eq. (1) of Ref. 37]:

$$\frac{d[Xe_2^+]}{dt} = +a[Xe]^2[Xe^+] - \alpha n_e[Xe_2^+] + \frac{\sigma_i I}{\hbar\omega}[Xe_2^*] - \frac{\sigma_{PD} I}{\hbar\omega}[Xe_2^+] \quad (15)$$

where a is the rate constant ($cm^6 s^{-1}$) for dimerization of Xe^+ to form Xe_2^+, α is the electron-Xe_2^+ dissociative recombination coefficient (expressed in $cm^3 s^{-1}$), I is the intensity of the *second* laser pulse, n_e is the electron density, the square brackets denote the density of the species in the bracket, and σ_i and σ_{PD} are the Xe_2^* photoionization and Xe_2^+ $1(\frac{1}{2})_u \rightarrow 2(\frac{1}{2})_g$ photodissociation cross sections, respectively. While the second optical field is present, the first two terms on the right-hand side of (15) are negligible and so

$$\frac{d[Xe_2^+]}{dt} = -\frac{I}{\hbar\omega}(\sigma_{PD}[Xe_2^+] - \sigma_i[Xe_2^*]) . \quad (16)$$

Therefore, the rate of decline of the Xe_2^+ number density resulting from photodissociation of the ion will be determined by the relative magnitudes of the two terms inside the brackets. Referring to Fig. 7, the populations of the Xe($6p$) and Xe_2^* species peak at $\sim$100 and 400 ns, respectively. On the basis of Eq. (16), therefore, one would expect that the magnitude of the Xe $6p \rightarrow 6s$ fluorescence suppression would change as the time delay between the two lasers is varied. Table IV shows that this indeed occurs and that the maximum contribution to Xe_2^+ production by photoionization *is* observed for $\Delta t = 400$ ns when the Xe_2^* population has reached maximum. Also as expected, the fluorescence suppression is largest at $\Delta t = 100$ ns (when the Xe_2^+ population is large and the Xe_2^* density negligible) and increases again past $\sim$400 ns. These measurements were made with an ArF laser and a second excimer laser whose wavelength was 308 nm and $I_{XeCl} = 4$ MW cm^{-2} ($\Phi = 6.7 \times 10^{16}$ cm^{-2}).

Finally, the measured values for N* in Table III further reinforce the conclusion that Xe_2^* is being photoionized. Computer modeling of the Xe_2^+-Xe*-Xe_2^* system[24] predicts atomic excited state densities that are at least 2 orders of magnitude smaller than the molecular excited-state populations measured here.

TABLE IV. Suppression of Xe $6p \rightarrow 6s$ fluorescence ($\lambda = 828$ nm) as a function of the time delay (Δt) between the two laser pulses ($p_{Xe} = 300$ Torr, $I_{ArF} = 130$ MW cm^{-2}, $I_{XeCl} = 4.0$ MW cm^{-2}).

Δt (ns)	Fractional fluorescence[a]
100	0.69±0.02[b]
400	0.87±0.04
800	0.82±0.03
1200	0.80±0.04

[a]See Eq. (13), Ref. 37 for a definition of fractional fluorescence.
[b]Uncertainty represents one standard deviation in the data.

B. Relevant molecular transitions

Referring back to Fig. 2, Xe $6s[\frac{3}{2}]_{1,2}$ atoms combine with the ground-state species to give rise to a number of bound and dissociative molecular states. The curves shown in Figs. 2 and 10 are those calculated by Ermler *et al.*[29] invoking the self-consistent field approximation and include relativistic effects. Experimental studies[38–40] of the Xe_2^* 0_u^+ and 1_u states have also been carried out by absorption spectroscopy and the results agree well with the theoretical curves shown in the figures. Virtually no experimentally-derived information is available for the higher-lying excited states.

The question that must be asked now is, if the atomic Xe populations peak too early in time to account for the observed increase in the photoelectron density, what molecular states are involved? The photoionization cross sections obtained from this experiment indicate that an Xe_2^* (1_g or 2_g) level is being ionized at all wavelengths except 248 nm, where the 0_u^+ (and possibly 0_u^- or 1_u) level becomes involved. This conclusion is based on several observations. Note first from Fig. 2 that, of the five wavelengths studied, only a KrF laser photon ($\lambda = 248.4$ nm, $\hbar\omega \simeq 5$ eV) is sufficiently energetic to ionize the lowest 0_u^+ state. Assuming that all optical transitions must be $u \leftrightarrow g$, the first available molecular ion state is $1(\frac{3}{2})_g$. Accessing this state from the lowest 0_u or 1_u states requires that $\hbar\omega \gtrsim 5$ eV (assuming that the population of the initial or lower level is thermally equilibrated). Said another way, the second laser wavelength may be no longer than $\sim$264 nm if photoionization on the $0_u^+ \rightarrow 1(\frac{3}{2})_g$ transition is to be realized.

Secondly, recall that the saturated electron-density (equivalent to N*) values for $\lambda = 351$, 337, 308, and 277 nm are approximately equal which suggests that the same excimer state is being photoionized at these wavelengths. Therefore, we turn our attention to the lowest-lying set of gerade states, the 1_g and 2_g levels which, though not bound as strongly as the 0_u^-, 1_u, and 0_u^+ states, are still quite stable and presumably not optically connected to ground (0_g^+).[38] Furthermore, the 1_g and 2_g states can be photoionized [via the $Xe_2^*(1,2)_g \rightarrow Xe_2^+$ $1(\frac{1}{2})_u$ transition] at wavelengths as long as 370 nm ($\hbar\omega_{MIN} \sim 3.4$ eV). For wavelengths below roughly 318 nm, the $1(\frac{3}{2})_u$ state of the molecular ion is also accessible.

At 248 nm, the saturated electron density is $\approx$60% of that measured at the other wavelengths which indicates that the initial state changes between $\lambda = 277$ and 248 nm. The radical decline in the magnitude of the cross section between the two wavelengths also seems to bear this out. Therefore, while it is impossible to be dogmatic, the large populations that one would expect in the lowest-lying u and g states and the two different values of Δn_e do suggest that photoionization of the 1_g and 2_g states of Xe_2^* predominates for $\lambda \gtrsim 250$ nm while at 248 nm, the transition involved is probably Xe_2^* $0_u^+ \rightarrow Xe_2^+$ $1(\frac{3}{2})_g$.

C. Comparison of experimental cross sections with theoretical values

To our knowledge, no experimental data exist in the literature with which to compare the results reported here. However, Fig. 9 does show the cross-sectional values calculated by Lorents *et al.* for the lowest-lying [$^3\Sigma(0_u^-, 1_u)$ and $^1\Sigma(0_u^+)$] states of Xe_2^* using a quantum-defect formalism.[22] While the two values are within a factor of 2 of each other at 308 nm ($\hbar\omega = 4$ eV), the discrepancy increases with the photon energy until at 248 nm, the cross sections differ by over an order of magnitude. Flannery and McCann[41] have also calculated the cross sections for *electron-impact* ionization of Xe_2^* ($^1\Sigma$ and $^3\Sigma$) and their 5-eV value (1.3×10^{-15} cm^2) is considerably larger than the value reported here for photoionization at 248 nm ($\hbar\omega\simeq5$ eV). The reason for the peak in the experimental cross section lying near 308 nm is not clear but may be related to the comment made previously that the long-wavelength threshold for the $1_g,2_g\rightarrow Xe_2^+\ 1(\frac{3}{2})_u$ transition lies in this spectral region.

Also presented in Fig. 9 are the results of quantum-defect calculations made by Hartquist[16] of the photoionization cross sections for the $6s[\frac{3}{2}]_2$ and $6s'[\frac{1}{2}]_0$ (i.e., lowest-lying metastables) states of atomic Xe. Although these calculations were specifically aimed at atomic levels, Hartquist claims that[16] "...the photoionization cross sections for He_2 should be similar to those for He. Similar arguments apply to the heavier rare gases and we expect the atomic and excimer cross sections to be approximately equal." Hartquist's own cross sections are displayed in Fig. 9, rather than other available data,[14,17] primarily because of his use of the *j-l* coupling formalism to describe the Xe* states. Considering both the magnitude and shape of the cross-section profile, the discrepancies between the experimentally-measured cross sections and those determined theoretically by Hartquist for the Xe* $6s[\frac{3}{2}]_2$ level and by Lorents *et al.* for Xe_2^* are roughly the same.

Of particular interest to this discussion, however, are the *ab initio* calculations of the Ar_2^* ($^1\Sigma_u^+$) photoionization cross-section spectrum published by Rescigno *et al.*[23] These are (to our knowledge) the only known *ab initio* studies yet done for R_2^* photoionization and, due to the rigor and detail (i.e., basis sets chosen) inherent with this approach, the cross-section spectral profile reported in Ref. 23 serves as a good reference against which the present results may be compared. Their value for the peak photoionization cross section ($\sim10^{-16}$ cm^{-2}) is roughly an order-of-magnitude larger than the largest value reported here for Xe_2^*. However, their photoionization profile and the data of Fig. 9 exhibit almost uncanny similarities in the photon energy corresponding with the peak cross section ($\hbar\omega\sim4$ eV) and in the shape of the curves (i.e., falling off more slowly to longer wavelengths).

VI. CONCLUSIONS

Absolute photoionization cross sections for the lowest bound excited states of the Xe dimer have been measured at several wavelengths in the ultraviolet. At 248 nm, photoelectrons are produced primarily by ionization of the 0_u^+ (and possibly 0_u^- or 1_u) state while at $\lambda=277$, 308, 337, and 351 nm, the dominant molecular transition appears to be $Xe_2^*\ (1_g,2_g)\rightarrow Xe_2^+\ 1(\frac{1}{2}$ or $\frac{3}{2})_u$. The cross sections reported here are in "order-of-magnitude" agreement with theoretical values published in 1973 and the measured photoionization profile is remarkably similar to that calculated for $Ar_2^*(^1\Sigma)$ by Rescigno *et al.*

The measured cross sections are quite large and have a clear impact on the operation of high-pressure gas lasers which contain Xe and operate in this spectral range. Foremost among these are, of course, the XeCl (308 nm) and XeF (351 nm) lasers themselves. The effect is the greatest for XeCl since the photoionization cross section at 308 nm is more than twice that at 351 nm.

In conclusion, it should be mentioned that photodissociation of the Xe_2^* (0_u^-,0_u^+, and $1g$) states is almost certainly also occurring in these experiments but the present apparatus is not designed to detect this process. Note from Fig. 2 that transitions from the lowest 0_u^- (or 1_u) state of Xe_2^* to the highest 0_g^+ level shown (associated with the $6s'[\frac{1}{2}]_1$ limit) requires photon energies in the range $3.0\lesssim\hbar\omega\lesssim3.8$ eV—precisely the region studied here. Such a process almost certainly also has a deleterious effect on excimer laser performance. Secondly, with the experimental approach outlined here, it should be possible to examine other, more highly excited states of Xe_2^* by combining a tunable dye laser with the microwave-absorption system.

ACKNOWLEDGMENTS

The authors wish to thank D. B. Geohegan for many stimulating discussions and helpful suggestions. Also, the excellent technical assistance of K. Kuehl, Y. Moroz, A. B. Wilson, Mrs. D. Watterson, and Mrs. K. Flessner is appreciated. A. W. M. acknowledges the partial financial support of the University of Illinois as a visiting research associate and M. N. E. gratefully acknowledges a Bell Laboratories Fellowship. This work was supported by the National Science Foundation (R. E. Rostenbach) under Grants Nos. CPE-82-07868 and CPE-82-19295.

[1] L. F. Champagne, in *Applied Atomic Collision Physics,* (Academic, New York, 1982), Vol. 3, pp. 349–386.
[2] R. F. Stebbings, F. B. Dunning, F. K. Tittel, and R. D. Rundel, Phys. Rev. Lett. 30, 815 (1973).
[3] F. B. Dunning and R. F. Stebbings, Phys. Rev. Lett. 32, 1286 (1974).
[4] R. F. Stebbings and F. B. Dunning, Phys. Rev. A 8, 665 (1973).
[5] F. B. Dunning and R. F. Stebbings, Phys. Rev. A 9, 2378 (1974).
[6] R. F. Stebbings, F. B. Dunning, and R. D. Rundel, in *Proceedings of the Fourth International Conference on Atomic Physics,* edited by G. zu Putlitz, E. W. Weber, and A. Winnaker (Plenum, New York, 1975), pp. 713–730.
[7] R. D. Rundel, F. B. Dunning, H. C. Goldwire, Jr., and R. F. Stebbings, J. Opt. Soc. Am. 65, 628 (1975).
[8] J. Bokor, J. Zavelovich, and C. K. Rhodes, Phys. Rev. A 21,

1453 (1980).
[9]S. S. Huang, Astrophys. J. 108, 354 (1948).
[10]A. Burgess and M. J. Seaton, Mon. Notic. R. Astron. Soc. 120, 121 (1960).
[11]D. W. Norcross, Proc. Phys. Soc. London, Sect. B 4, 652 (1971).
[12]A. Dalgarno, H. Doyle, and M. Oppenheimer, Phys. Rev. Lett. 29, 1051 (1972).
[13]H. A. Hyman, Appl. Phys. Lett. 31, 14 (1977).
[14]K. J. McCann and M. R. Flannery, Appl. Phys. Lett. 31, 599 (1977).
[15]A. U. Hazi and T. N. Rescigno, Phys. Rev. A 16, 2376 (1977).
[16]T. W. Hartquist, J. Phys. B 11, 2101 (1978).
[17]C. Duzy and H. A. Hyman, Phys. Rev. A 22, 1878 (1980).
[18]M. A. Pindzola, Phys. Rev. A 23, 201 (1981).
[19]T. N. Chang and Y. S. Kim, Phys. Rev. A 26, 2728 (1982).
[20]E. W. McDaniel, M. R. Flannery, E. W. Thomas, H. W. Ellis, K. J. McCann, S. T. Manson, J. W. Gallagher, J. R. Rumble, E. C. Beaty, and T. G. Roberts, U. S. Army Missile Research and Development Command, Redstone Arsenal, Alabama, Technical Report No. H-78-1, 1979 (unpublished), Vol. V.
[21]M. McCusker, in *Excimer Lasers,* edited by C. K. Rhodes (Springer, Berlin, 1979), p. 52; see also C. A. Brau, *ibid.*, p. 95.
[22]D. C. Lorents, D. J. Eckstrom, and D. Huestis, Stanford Research Institute Report No. MP-73-2, 1973 (unpublished).
[23]T. N. Rescigno, A. U. Hazi, and A. E. Orel, J. Chem. Phys. 68, 5283 (1978).
[24]A. W. McCown, M. N. Ediger, S. M. Stazak, and J. G. Eden, Phys. Rev. A 28, 1440 (1983); A. W. McCown, M. N. Ediger, and J. G. Eden, in *Excimer Lasers 1983,* edited by C. K. Rhodes, H. Egger, and H. Pummer (American Institute of Physics, New York, 1983), pp. 128–141 and 222–235.
[25]A. W. McCown, M. N. Ediger, and J. G. Eden, Phys. Rev. A 26, 3318 (1982).
[26]A. W. McCown, M. N. Ediger, and J. G. Eden, Phys. Rev. A 26, 2281 (1982).
[27]S. D. Rockwood, J. Appl. Phys. 45, 5229 (1974) and references cited therein. The electron temperature e^{-1} relaxation time is $(M/2m\nu_m)\simeq 3\ \mu$s where ν_m is the electron-neutral collision frequency.
[28]L. S. Frost and A. V. Phelps, Phys. Rev. 136, A1538 (1964).
[29]W. C. Ermler, Y. S. Lee, K. S. Pitzer, and N. W. Winter, J. Chem. Phys. 69, 976 (1978).
[30]H. Horiguchi, R. S. F. Chang, and D. W. Setser, J. Chem. Phys. 75, 1207 (1981).
[31]A. Gedanken, J. Jortner, B. Raz, and A. Szöke, J. Chem. Phys. 57, 3456 (1972).
[32]O. Cheshnovsky, B. Raz, and J. Jortner, J. Chem. Phys. 59, 3301 (1973).
[33]N. Sadeghi and J. Sabbagh, Phys. Rev. A 16, 2336 (1977).
[34]C. A. Brau, in *Excimer Lasers,* edited by C. K. Rhodes (Springer, Berlin, 1979), Table 4.7, p. 103.
[35]Y.-J. Shiu, M. A. Biondi, and D. P. Sipler, Phys. Rev. A 15, 494 (1977).
[36]R. S. Mulliken, J. Chem. Phys. 52, 5170 (1970).
[37]A. W. McCown, M. N. Ediger, and J. G. Eden, Phys. Rev. A 28, 3365 (1983).
[38]O. Dutuit, M. C. Castex, J. Le Calvé, and M. Lavollée, J. Chem. Phys. 73, 3107 (1980); M. C. Castex, *ibid.* 74, 759 (1981) and references cited therein.
[39]J. B. Gerardo and A. W. Johnson, Phys. Rev. A 10, 1204 (1974).
[40]D. A. Emmons, Opt. Commun. 11, 257 (1974).
[41]M. R. Flannery and K. J. McCann, Air Force Wright Aeronautical Laboratories (Wright-Patterson Air Force Base, OH), Technical Report No. AFWAL-TR-80-2015, 1980 (unpublished), p. 33.

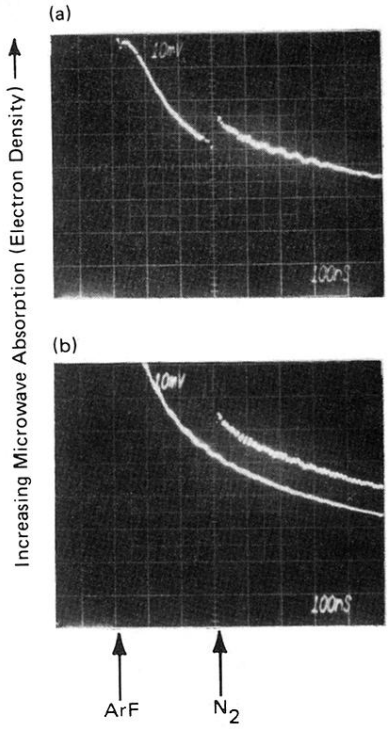

FIG. 3. Typical microwave-absorption oscillograms for 300 Torr of Xe irradiated initially by ArF (193 nm) followed ~ 300 ns later by an N_2-laser (337 nm) pulse. Photograph (a) shows the entire waveform and two waveforms are superimposed in (b)—one showing the effect of both laser pulses and a second associated with only the 193-nm beam. Microwave absorption (and, hence, electron density) increases vertically. The ArF pulse produces a peak electron density of $\sim 2.4\times 10^{13}$ cm^{-3} and 3.0×10^{13} cm^{-3} for (a) and (b), respectively, and the N_2 laser radiation leads to an instantaneous jump in the electron density. The ArF and N_2 laser intensities are 90 and 12 MW cm^{-2}, respectively, in (a) and 100 and 16 MW cm^{-2} ($E_{N_2} \cong 10$ mJ, $\Phi_{N_2} = E_{N_2}(\hbar\omega A)^{-1} = 2.2\times 10^{17}$ cm^{-2}) in (b).